International Journal of Nanoelectronics and Materials
IJNeaM
ISSN 1985-5761 | E-ISSN 2232-1535

# First principle method for studying thermoelectric properties of anti-perovskite $Ba_3SiO$ and $Ca_3SiO$ compounds

Muhammad Sholihin A. Rahim [a,b,c] *, Abdullah Chik [a,b,c], Yeoh Cheow Keat [a,b,c], Ishak Jainoo [c], and Nur Aina Syafarina [a,b,c]

[a]*Center for Frontier Materials Research, Universiti Malaysia Perlis, 01000 Kangar, Perlis, Malaysia*
[b]*Center of Excellence Geopolymer and Green Technology (CEGeoGTech), Universiti Malaysia Perlis (UniMAP), 02600 Jejawi, Arau, Perlis, Malaysia*
[c]*Faculty of Chemical Engineering & Technology, Taman Muhibbah School Complex 2, 02600 Jejawi, Arau, Perlis, Malaysia*
*∗Corresponding author. Tel.: +60175430797; e-mail: msholihin555@gmail.com*

Received 4 December 2025, Revised 22 January 2026, Accepted 10 February 2026

**ABSTRACT**

Thermoelectric materials, which utilize a temperature gradient to convert heat energy into electrical energy, hold immense promise for power generation. The efficiency of such compounds is mainly measured by their figure of merit (*ZT*), which indicates their efficiency to convert heat energy to electrical energy. This study investigated the potential of anti-perovskite $Ba_3SiO$ and $Ca_3SiO$ compounds as thermoelectric materials. The Boltzmann transport equation (BTE) was utilized using the BoltzTraP code to evaluate the transport and thermoelectric properties of $Ba_3SiO$ and $Ca_3SiO$ compounds. The electronic properties including, the band structure and density of states (DOS) were computed using CASTEP code using the generalized gradient approximation with the Perdew-Burke-Ernzerhof (GGA-PBE) functional. Results showed that both $Ba_3SiO$ and $Ca_3SiO$ are direct band gap semiconductor materials at the Γ - Γ k-points with band gaps values of 0.44 eV for $Ba_3SiO$ and 0.11 eV for $Ca_3SiO$. In addition, we found that the figure of merit at room temperature was determined to be higher for $Ca_3SiO$ compared to $Ba_3SiO$, with values of $2.50 \times 10^{-2}$ and $9.66 \times 10^{-4}$, respectively. This indicates that substituting of X cation from Ba to Ca in the $X_3SiO$ compound enhances in the thermoelectric performance.

**Keywords:** *Density functional theory, Anti-perovskites, Thermoelectric properties, Semiconductor materials*

## 1. INTRODUCTION

Thermoelectric (TE) technology is a method for harvesting heat energy and convert it into electrical energy in thermoelectric generator [1]. This conversion relies on a temperature difference across the material, which is a phenomenon known as Seebeck effect. TE materials are increasingly utilized in applications such as solar thermal systems, wearable devices, temperature sensors, and gas sensors [2]. The performance of TE materials is often assessed using the figure of merit (Equation (1)) [3]:

$$ZT = \frac{S^2 \sigma T}{k_{total}} \quad (1)$$

where figure of merit (*ZT*) comprises the Seebeck coefficient (*S*), electrical conductivity ($\sigma$), absolute temperature (*T*) and total thermal conductivity (*k*). The total thermal conductivity ($k_{total}$) is composed of electronic thermal conductivity ($k_{ele}$) and lattice thermal conductivity ($k_{lat}$) [4]. Anti-perovskites are structurally identical to perovskite materials, but differ in their arrangement of cations and anions. For anti-perovskite, the general formula is $X_3AB$, where A and B are anions, while X is a cation. Anti-perovskite oxides, a subclass of anti-perovskite family have been studied for their physical properties which highlights their significance for thermoelectric applications [5].

Historically, lead telluride (PbTe) compound has achieved a high *ZT* about 0.8 at 725 K [6]. Recent advancements in this compound have led to even higher *ZT* values that reach approximately 1.8 for PbTe-PbSe materials [7]. However, despite the advantage of a relatively high *ZT* value of PbTe, it poses environmental concerns because of its hazardous effect and relatively high price. Therefore, an extensive research has been undertaken to determine environmentally safer alternatives for thermoelectric materials. Scientists have explored the compounds includes oxides, carbides, nitrides, and sulfides that have the potential to be free from toxic substances [8–10].

In recent years, considerable research attention has been directed towards anti-perovskite oxides as potential thermoelectric materials because of their lower thermal conductivity. Zhao et al. reported that $Rb_3AuO$ displays a high *ZT* of 1.02 with a low lattice thermal conductivity of 0.7 at 300 K [11]. The anti-perovskite $Rb_3CuO$ and $Rb_3AgO$ have been theoretically examined for their thermoelectric applications. These compounds show indirect semiconductor behavior with band gaps of approximately 0.23 eV for $Rb_3CuO$ and 0.20 eV for $Rb_3AgO$ as determined via generalized gradient approximation with Perdew-Burke-Ernzerhof (GGA-PBE) functional. The high *ZT* with the value of 0.79 for both $Rb_3CuO$ and $Rb_3AgO$ at 400 K is related to the narrow band gaps, which are advantageous for thermoelectric applications [12].

In another recent theoretical study, He *et al.* has reported that $Ba_3SiO$ showed a band gap of 0.86 eV with semiconducting behaviour using the projector augmented wave (PAW) method incorporated into the Vienna ab initio Simulation Package (VASP) code using the Heyd-Scuseria-Enzerhof (HSE) hybrid functional. He *et al.* also mentioned that their band gap value is larger than experimental value of 0.63 eV [13]. The author also calculated the figure of merit for orthorhombic crystal structure of $Ba_3SiO$ with 0.16 at 300 K and predicted 2.14 at 600 K with varying concentrations from $10^{17}$ to $10^{21}$ $cm^{-3}$. Furthermore, Pohls *et al.* [14] studied $Ca_3SiO$, which have a similar structure to $Ba_3SiO$ and found that $Ca_3SiO$ has a band gap of 0.2 eV with semiconducting behavior using GGA-PBE with VASP code. Pohls *et al.* also calculated the resistivity and Seebeck coefficient for $Ca_3SiO$ in terms of varying concentrations from $10^{19}$ to $10^{20}$ $cm^{-3}$, and found that high electrical resistivity limits the thermoelectric potential of this compound. However, further study of thermoelectric properties of intrinsic $Ba_3SiO$ and $Ca_3SiO$ is needed to verify these predictions.

In this work, the thermoelectric properties of anti-perovskite $Ba_3SiO$ and $Ca_3SiO$ compounds were investigated using the density functional theory (DFT) method and Vanderbilt ultrasoft pseudopotential incorporated in the Cambridge Serial Total Energy Program (CASTEP) code [15] via generalized gradient approximation for calculating electronic and thermoelectric properties. Our analysis includes calculations of the Seebeck coefficient, electrical conductivity, thermal conductivity, and figure of merit to predict the effective performance of these compounds for thermoelectric applications. The correlation of X cations with thermoelectric properties was also discussed.

## 2. METHODOLOGY

In this work, both $Ba_3SiO$ and $Ca_3SiO$ crystallize in orthorhombic crystal structures with space group Pnma (No. 16) and Imma (No. 74), respectively. The electronic configuration used in the calculations was as follows: Ba: $5s^2$ $5p^6$ $6s^2$, Ca: $3s^2$ $3p^2$ $4s^2$, O: $2s^2$ $2p^4$, and Si: $3s^2$ $3p^2$. The density functional theory (DFT) was employed to compute thermoelectric properties of $Ba_3SiO$ and $Ca_3SiO$ using Boltzmann transport equation (BTE) within the BoltzTraP code [16]. This BoltzTraP code utilized output file from CASTEP, particularly file.bands and file.castep, which were converted using castep3boltz.py tools into file format, which can be used by BoltzTraP code. Moreover, the lattice thermal conductivity was calculated using phono3py code in Quantum Espresso (QE) with the k-point grid of $4 \times 4 \times 4$ and energy cut-off (ecutwfc) of 50 Ry for both $Ba_3SiO$ and $Ca_3SiO$ compounds. These values were selected to reduce the computational time, as QE and phono3py are computationally time-consuming. QE was used instead of CASTEP due to CASTEP does not support the required phonon-phonon interaction scheme. Phono3py [17] applied supercell approach to calculate force constants and then solves the BTE to calculate lattice thermal conductivity. The electronic band structure and density of state (DOS) were computed in CASTEP code. The exchange correlation energy was treated with the generalized gradient approximation with Perdew-Burke-Ernzerhof (GGA-PBE) functional [18], which is applicable for calculating the bulk materials of these compounds [19].

To ensure both accuracy and efficiency, we begin by optimizing the modelling parameters, such as the k-point and energy cut-off through a parameter optimization. This step was important for minimizing computational time and resources for the CASTEP calculations. After parameter optimization, the structures of $Ba_3SiO$ and $Ca_3SiO$ were further optimized using Broyden-Fletcher-Goldfarb-Shanno (BFGS) method to achieve structural stability. Once the optimized structures were obtained, we moved forward with the electronic and thermoelectric properties calculations. For these calculations, the optimized k-point grids of $5 \times 5 \times 3$ for $Ba_3SiO$ and $4 \times 4 \times 3$ for $Ca_3SiO$ were used in the Irreducible Brillioun Zone (IBZ). The plane energy cut-off with 600 eV and 700 eV for $Ba_3SiO$ and $Ca_3SiO$, respectively, were used to maximize the inclusion of plane wave sets in the CASTEP calculations.

## 3. RESULTS AND DISCUSSIONS

### 3.1. Structural Properties

The crystal structures of $Ba_3SiO$ and $Ca_3SiO$ are presented in Figure 1. These structures were optimized under geometry optimization with total energy calculations performed as a function of volume. The results were then fitted using the third order Birch-Murnagham equation [20]. Equation (2) can be expressed as follows:

$$P(V) = \frac{3}{2}B + \left[\left(\frac{V_o}{V}\right)^{\frac{7}{3}} - \left(\frac{V_o}{V}\right)^{\frac{5}{3}}\right] * \left\{1 + \frac{3}{4}(4 - B')\left[\left(\frac{V_o}{V}\right)^{\frac{2}{3}} - 1\right]\right\} \quad (2)$$

where *P(V)* represents the pressure as a function of volume, $V_o$ is the equilibrium volume, $B$ is the bulk modulus, $B_O'$ is the first derivative of the bulk modulus and $V$ is the volume at a given pressure. This fitting result provided optimized lattice parameters with structural stability. The calculated lattice parameters were obtained approximately at a = 7.525 Å, b = 7.802 Å, and c = 10.838 Å for $Ba_3SiO$, whereas for $Ca_3SiO$, the lattice parameters were a = 6.667 Å, b = 6.686 Å, and c = 9.443 Å. A comparison of these results with those of previous studies, revealed that the calculated lattice parameters in this study are in good agreement with the experimental and theoretical results by Huang & Corbett [21] and Mahmood *et al.* [22]. Moreover, the thermodynamic stability of these compounds was assessed through formation energy calculations by employing the following Equation (3) [23]:

$$\Delta f_E(X_3AB) = \frac{(E_{X_3AB} - N_A E_A - N_B E_B - N_x E_x)}{N_{tot}} \quad (3)$$

Here, $\Delta f_E(X_3AB)$ denotes the formation energy (eV), $E_{X_3AB}$ represents the total energy of $X_3AB$ compound, $N_{tot}$ is the

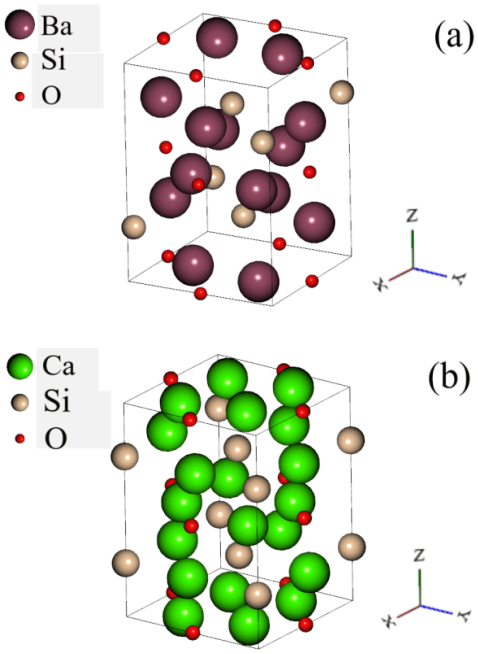


**Figure 1**. Crystal structures of
(a) $Ba_3SiO$ and (b) $Ca_3SiO$ compounds

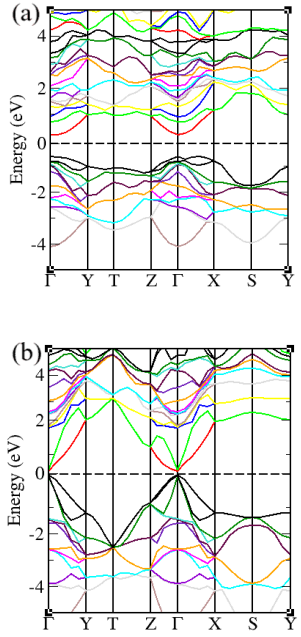


**Figure 2**. The band structures of
(a) $Ba_3SiO$ and (b) $Ca_3SiO$ compounds

total number of atomic sites, $E_A$ is the total energy of atom A, $E_B$ is the total energy of atom B and $E_X$ is the total energy of atom X. The negative formation energy indicates the stability of materials with the lowest energy state. In this work, $Ca_3SiO$ exhibited higher thermodynamic stability with a formation energy of –8.424 eV, whereas $Ba_3SiO$ shows relatively lower stability with a formation energy of –6.662 eV. Despite this difference, the negative formation energies of both compounds suggest that $Ba_3SiO$ and $Ca_3SiO$ are stable materials.

### 3.2. Electronic Properties

#### 3.2.1. Band Structure

The calculated band structures of $Ba_3SiO$ and $Ca_3SiO$ compounds is showed in Figure 2. From the band structure analysis, the band gaps of these compounds are 0.44 eV for $Ba_3SiO$ and 0.11 eV for $Ca_3SiO$. These results are close to other researcher's results such as Garcia-Castro *et al.* [24] who determined a band gap of 0.42 eV for $Ba_3SiO$ and Pohls *et al.* [14] who reported a band gap of 0.2 eV. From the Figure 2 also, we observed that the band gap of $Ba_3SiO$ is relatively larger compared to the narrow band gap of $Ca_3SiO$. This result shows that both $Ba_3SiO$ and $Ca_3SiO$ are semiconductor materials with the direct band gaps at the Γ - Γ k-points. The lower band gap of $Ca_3SiO$ is related to the lower ionic radius of Ca than that of Ba. The lower band gap of $Ca_3SiO$ also indicates to the higher transfer of charge carriers resulting in high carrier concentration at the Fermi level and increasing the electrical conductivity compared to wide band gap of $Ba_3SiO$.

#### 3.2.2. Density of States

The total density of states (TDOS) and partial density of states (PDOS) of $Ba_3SiO$ and $Ca_3SiO$ are showed in Figure 3. The TDOS plot highlights several distinct peaks, representing the number of available electron states at various energy ranges for these compounds. In the valence bands, from the range of –5 eV to 0 eV, the density of states is lower than that in the conduction bands, which lie between 0 eV to 5 eV. This lower density in the valence band occurs because most electron states are occupied by electrons. In contrast, the conduction band shows a higher electron density of states due to the greater number of unoccupied states, which are available for electron excitation.

The PDOS plot reveals that the Si-p state is mainly contributes to the valence band with sharp peaks near the Fermi level compared with O-p state, particularly in the energy range of –0.25 eV to 0.05 eV for $Ba_3SiO$ and –3.05 eV to 0.04 eV for $Ca_3SiO$. Furthermore, Ba-d/Ca-d and O-p states show some overlap with Si-p state in the valence

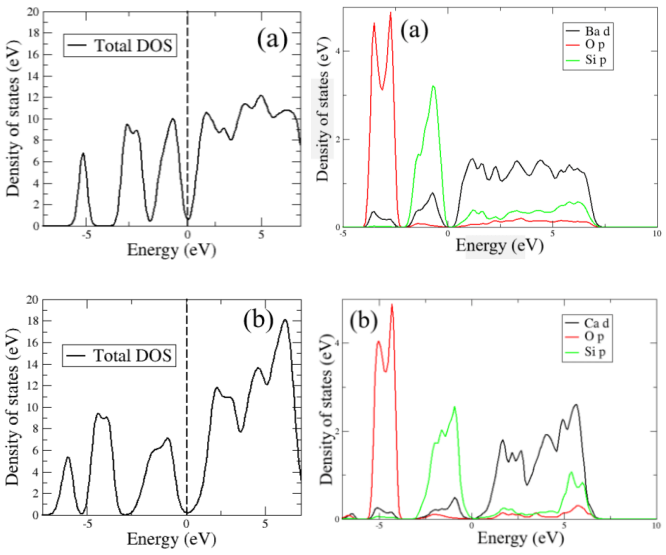


**Figure 3**. Total (left) and partial (right) density of states for
(a) $Ba_3SiO$ and (b) $Ca_3SiO$ compounds

band for these compounds. In the conduction band, Ba-d and Ca-d states are the primary contributors to this band, overlapping with smaller Si-p and O-p states near the Fermi level in the energy range of 0.25 eV to 7.27 eV for $Ba_3SiO$ and 0 eV to 6.72 eV for $Ca_3SiO$. The higher PDOS peak in the valence band that is closest to the Fermi level is related to Si-p state with values of 3.23 eV in $Ba_3SiO$ and 2.56 eV in $Ca_3SiO$ compared to Ba-d and Ca-d states in the conduction band. In the conduction band also, the highest PDOS peak nearest to the Fermi level is Ba-d state with a value of 1.56 eV in $Ba_3SiO$, whereas Ca-d state with a value of 1.81 eV in $Ca_3SiO$.

### 3.3. Thermoelectric Properties

#### 3.3.1. Seebeck Coefficient

The calculated Seebeck coefficient versus temperature for $Ba_3SiO$ and $Ca_3SiO$ is shown in Figure 4. At 300 K, the Seebeck coefficient for $Ba_3SiO$ is $-4.94 \times 10^{-4}$ V/K and it decreases to a value of $4.71 \times 10^{-5}$ V/K at 1000 K. The Seebeck coefficient provides information regarding to the dominant charge carrier in materials by showing negative Seebeck coefficient for n-type material and positive Seebeck for p-type material [25]. From 300 K to 650 K, the $Ba_3SiO$ has a negative Seebeck coefficient, which shows that it is an n-type material. However, from 700 K to 1000 K, the $Ba_3SiO$ changes to a p-type material, as proven by a positive Seebeck coefficient.

On the other hand, $Ca_3SiO$ shows a Seebeck coefficient of $1.51 \times 10^{-4}$ V/K at 300 K. From Figure 4 also, the Seebeck coefficient showed gradually decreases as the temperature increases, reaching a value of $8.46 \times 10^{-5}$V/K at 1000 K. From 300 K to 1000 K, $Ca_3SiO$ has a positive Seebeck coefficient, indicating that it is a p-type material. The lower Seebeck coefficient of $Ca_3SiO$ is related to its higher carrier concentration at the Fermi level than that of $Ba_3SiO$, as the carrier concentration is inversely proportional to the Seebeck coefficient.

Based on Seebeck analysis, $Ba_3SiO$ has a greater Seebeck coefficient in magnitude from 300 K to 1000 K than $Ca_3SiO$ does. This occurs because the carrier concentration at the Fermi level for $Ba_3SiO$ is lower, ranging from $-3.4 \times 10^{16}$ $cm^{-3}$ to $1.43 \times 10^{19}$ $cm^{-3}$ than that for $Ca_3SiO$, which ranges from $3.04 \times 10^{18}$ $cm^{-3}$ to $1.53 \times 10^{19}$ $cm^{-3}$ from 300 K to 1000 K, as shown in Figure 5.

#### 3.3.2. Correlation of X Cations with Seebeck Coefficient

Figure 6 show the correlation of X cations with Seebeck coefficient for $Ba_3SiO$ and $Ca_3SiO$ compounds. The variation in X cations influences the carrier type from 300 K to 1000 K. The substitution of X cations for $Ba^{+2}$ results in the transition from n-type conduction to p-type conduction, while for $Ca^{+2}$, the substitution of this cation results in p-type conduction. From the Seebeck coefficient analysis, the substitution of $Ba^{2+}$, results in the highest Seebeck coefficient (in magnitude) for $Ba_3SiO$ from 300 K to 600 K, which related with its lowest carrier concentration, as shown in Figure 5.

On the other hand, the substitution of $Ca^{2+}$ exhibits lowest Seebeck coefficient (in magnitude) corresponding to its higher carrier concentration from 300 K to 1000 K. These trends align with the simple models of electron transport formula (Equation (4)) as [26]:

$$S = \frac{8\pi^2 K_B^2 T}{3eh^2} m^* \left(\frac{\pi}{3n}\right)^{2/3} \quad (4)$$

where $n$, $h$, $m^*$, $e$, $K_B$ denotes the carrier concentration, the density of states (DOS), effective mass of charge carrier, Planck's constants, carrier charge, and Boltzmann constant, respectively. This relationship shows that Seebeck coefficient is inversely related to carrier concentration, given by $S \propto 1/n$. Regard to carrier concentration, the narrow band gap of $Ca_3SiO$, as shown in Figure 2, allows for greater electron excitation across the Fermi level, thereby increasing the carrier concentration.

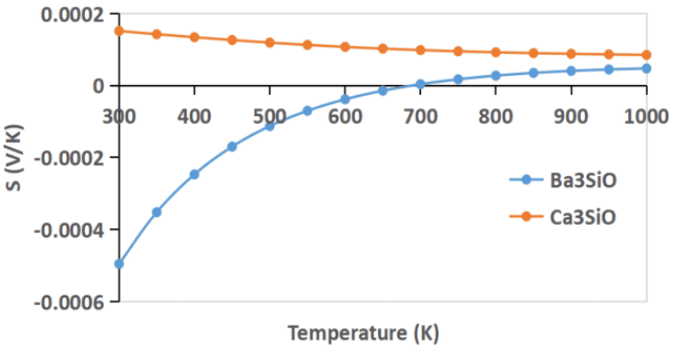


**Figure 4**. Calculated Seebeck coefficient of $Ba_3SiO$ and $Ca_3SiO$ compounds

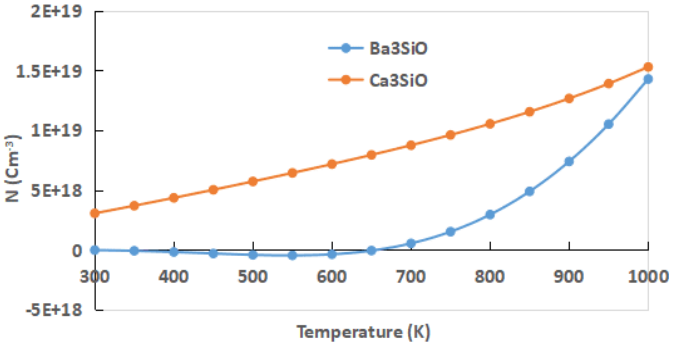


**Figure 5**. Calculated carrier concentration of $Ba_3SiO$ and $Ca_3SiO$ compounds

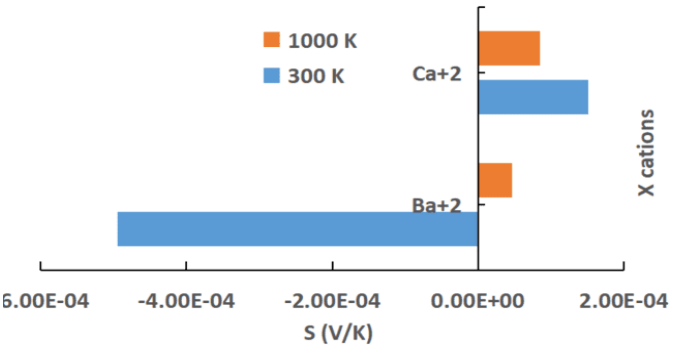


**Figure 6**. Correlation of X cations with Seebeck coefficients of $Ba_3SiO$ and $Ca_3SiO$ compounds

### 3.3.3. Electrical Conductivity

The calculated electrical conductivity of $Ba_3SiO$ and $Ca_3SiO$ are presented in Figure 7. In BoltzTrap code, electrical conductivity was calculated using constant time relaxation (CTR), which refers to $\sigma/\tau$. Usually, the electrical conductivity of these compounds were multiplied with $\tau$, to obtain the σ value. The method to calculate these conductivities also reported by Xiong *et al.* [27]. In this study, these conductivities were calculated using the value $\tau$ of $0.8 \times 10^{-15}$ s, which have been reported by Shamim *et al.* in their work for calculating metal and degenerate semiconductor [28]. The calculated electrical conductivity of these compound is obtained from $\sigma/\tau \times \tau$. Both compounds show an increase in conductivity with temperature increase from 300 K to 1000 K. At room temperature, $Ca_3SiO$ has a higher electrical conductivity of 5610 $(\Omega \cdot m)^{-1}$ than $Ba_3SiO$ with a value of 12 $(\Omega \cdot m)^{-1}$. Whereas, at 1000 K, $Ca_3SiO$ shows the higher conductivity value of 41378 $(\Omega.m)^{-1}$ compared to $Ba_3SiO$ with the value of 11359 $(\Omega \cdot m)^{-1}$.

### 3.3.4. Correlation of X Cations with Electrical Conductivity

Figure 8 presents the correlations of X cations with electrical conductivity of $Ba_3SiO$ and $Ca_3SiO$ compounds. The substitution of X cations from $Ba^{+2}$ to $Ca^{+2}$ exhibit increasing trend of electrical conductivity from 300 K to 1000 K. Among these compounds, $Ca_3SiO$ shows the higher electrical conductivity, whereas $Ba_3SiO$ shows the lowest electrical conductivity for these temperatures.

This observed trend can be explained by the band gap of this compound. The smaller band gap in $Ca_3SiO$ facilitates the mobility of electrons across the Fermi level, which requires less energy for electrons to jump from the valence band to the conduction band compared to $Ba_3SiO$, which has a wide band gap. Therefore, the charge carrier mobility in $Ca_3SiO$ is greater than that in $Ba_3SiO$, resulting in increased electrical conductivity. This result follows the electrical conductivity in semiconductor that expressed as Equation (5) [29]:

$$\sigma = ne \tag{5}$$

where n, e, and μ represents carrier concentration, carrier charge, and carrier mobility, respectively. This formula shows that the electrical conductivity is directly dependent on the carrier concentration.

### 3.3.5. Electronic and Lattice Thermal Conductivity

The output electronic thermal conductivity of these compounds is obtained using the BoltzTraP code, with the value of $k_{ele}/\tau$. To determine the final $k_{ele}$ values, the results from BoltzTraP code are multiply by the $\tau$. Figure 9 show the calculated electronic thermal conductivity of $Ba_3SiO$ and $Ca_3SiO$ compounds. Both compounds exhibit an increasing trend from 300 K to 1000 K. At 300 K, the electronic thermal conductivity values for $Ba_3SiO$ and $Ca_3SiO$ are $2.45 \times 10^{-3}$ W/mK and 0.13 W/mK, respectively. These values increased with temperature, reaching the peak values of 2.07 W/mK for $Ba_3SiO$ and 3.88 W/mK for $Ca_3SiO$ at 1000 K. The number of thermally excited charge carriers increased when the temperature increased. As a consequece, the electronic thermal conductivity increased with increases in the mobility of free electrons in the crystal [30]. The higher electronic conductivity is also related to the higher electrical thermal conductivity. This trend follows the Wiedemann-Franz law, which states that the electronic thermal conductivity ($k_{ele}$) is directly proportional to electrical conductivity ($\sigma$) with the formula of $k_{ele} = L\sigma T$ [31].

Figure 10 presents the calculated lattice thermal conductivity of $Ba_3SiO$ and $Ca_3SiO$ compounds. The $Ca_3SiO$ shows the highest lattice thermal conductivity from 300 K to 1000 K with the values of 1.39 W/mK to 0.46 W/mK, respectively, whereas $Ba_3SiO$ demonstrates lowest lattice thermal conductivity values of 0.91 W/mK at 300 K to

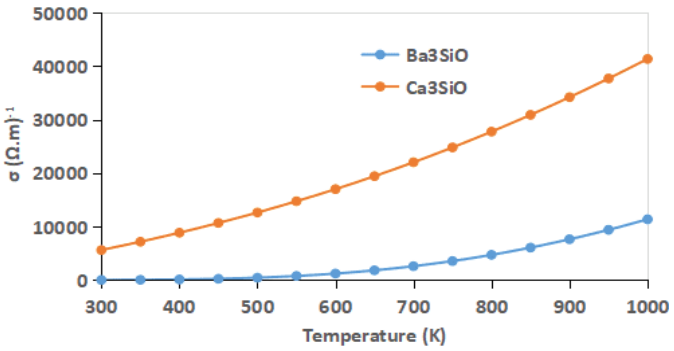


**Figure 7**. Calculated electrical conductivity of $Ba_3SiO$ and $Ca_3SiO$ compounds

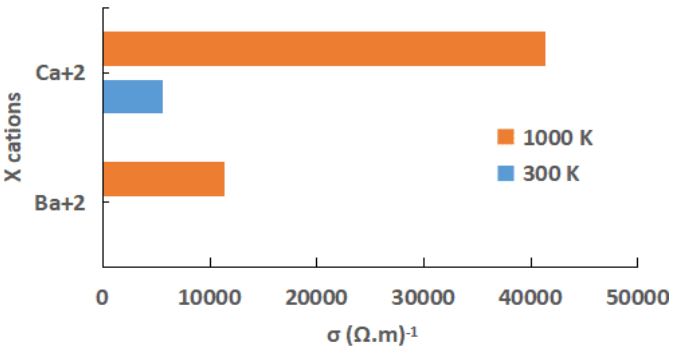


**Figure 8**. Correlation of X cations with Seebeck coefficient of $Ba_3SiO$ and $Ca_3SiO$ compounds

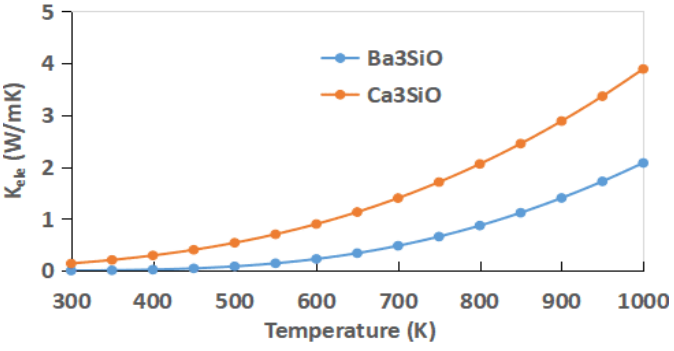


**Figure 9**. Calculated electronic thermal conductivity of $Ba_3SiO$ and $Ca_3SiO$ compounds

0.28 W/mK at 1000 K. These compounds show a decreasing trend as temperature increases. This behavior is common for various materials because the heat transfer is impeded by increased phonon scattering at high temperature.

### 3.3.6. Total Thermal Conductivity

The total thermal conductivity of these compounds are obtained by summing the electronic thermal conductivity and lattice thermal conductivity. Figure 11 shows the calculated total thermal conductivity ($k_{total}$) of $Ba_3SiO$ and $Ca_3SiO$ compounds. The thermal conductivity of both compounds gradually increases with temperature, reaching the highest value at 1000 K. At 300 K, the thermal conductivity of $Ba_3SiO$ is 0.917 W/m·K, while $Ca_3SiO$ shows a higher value of 1.53 W/m·K. As the temperature rises to 1000 K, the values increase to 2.35 W/m.K for $Ba_3SiO$ and 4.35 W/m·K for $Ca_3SiO$. The narrow band gap and the small ionic radius of Ca contributes significantly to the increasing thermal conductivity. The narrow band gap promotes the excitation of charge carriers to mobilize in the material. These excitation charge carriers mobility enhance the electrical conductivity, which facilitates increasing heat transfer, thereby increasing the thermal conductivity.

From total thermal conductivity analysis, $Ba_3SiO$ has the lowest total thermal conductivity compared with $Ca_3SiO$ at 300 K. In thermoelectric applications, $Ba_3SiO$ is preferable because of its low total thermal conductivity, which helps to minimize heat loss and enhances the efficiency of converting heat energy into electrical energy [32].

### 3.3.7. Correlation of X Cations with Total Thermal Conductivity

Figure 12 show the correlation of X cations with the total thermal conductivity of $Ba_3SiO$ and $Ca_3SiO$ compounds. The bar graph in relationship of X cations with thermal conductivity shows increasing trend when substitutes $Ba^{+2}$ to $Ca^{+2}$ from 300 K to 1000 K. In general, mobile electrons carry the electrical charge and heat energy, resulting in a higher electron carrier concentration for $Ca^{+2}$. As a consequence, the electrical conductivity increased with the thermal conductivity in $Ca_3SiO$ compared to $Ba_3SiO$. For both compounds, the increases in electronic thermal conductivity contributed to total thermal conductivity compared to lattice thermal conductivity.

### 3.3.8. Figure of Merit

The efficiency of thermoelectric materials is described by a figure of merit. Figure 13 shows the figure of merit for $Ba_3SiO$ and $Ca_3SiO$ compounds. The efficiency of thermoelectric materials is described by a figure of merit. The *ZT* curve of $Ba_3SiO$ exhibit increasing trend from 300 K to 450 K with values of $9.66 \times 10^{-4}$ to $4.5 \times 10^{-3}$. However, at 450 K, the *ZT* curve of this compound decreased from 500 K to 700 K with the values of $4.34 \times 10^{-3}$ to $2.26 \times 10^{-5}$, respectively. At 750 K with the value of $7.36 \times 10^{-4}$, the *ZT* curve increased sharply to value of $1.06 \times 10^{-2}$ at 1000 K.

For $Ca_3SiO$, the *ZT* curve exhibits increasing trend from 300 K to 600 K and then decreased to point at 1000 K. From

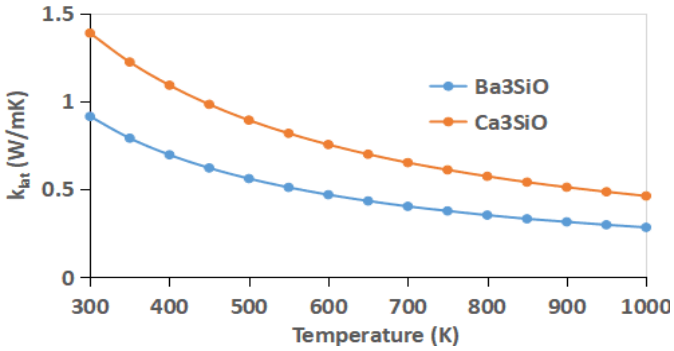


**Figure 10**. Calculated lattice thermal conductivity of $Ba_3SiO$ and $Ca_3SiO$ compounds

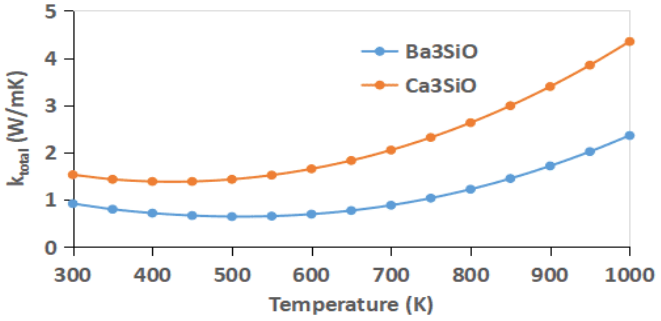


**Figure 11**. Calculated total thermal conductivity of $Ba_3SiO$ and $Ca_3SiO$ compounds

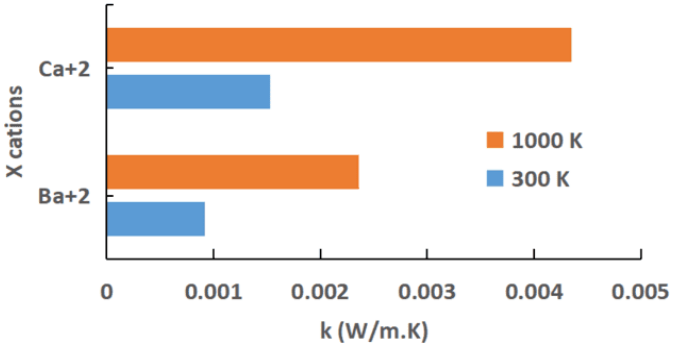


**Figure 12**. Correlation of X cations with thermal conductivity of $Ba_3SiO$ and $Ca_3SiO$ compounds

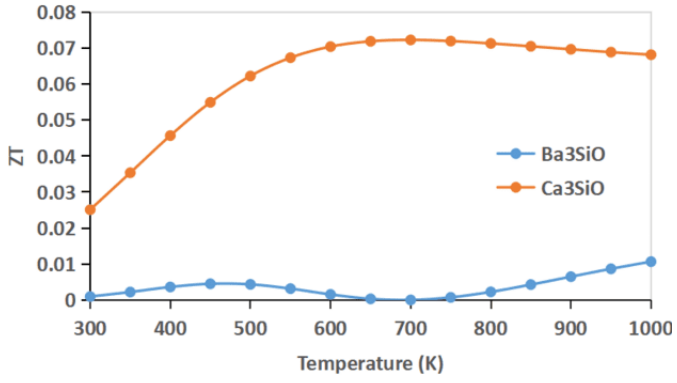


**Figure 13**. Calculated figure of merit for $Ba_3SiO$ and $Ca_3SiO$ compounds

300 K to 600 K, the *ZT* curve increases sharply with the value of $2.50 \times 10^{-2}$ to $7.03 \times 10^{-2}$, respectively. Nevertheless, from 650 K to 1000 K, the *ZT* curve decreased from $7.18 \times 10^{-2}$ to $6.81 \times 10^{-2}$, respectively. From *ZT* analysis, $Ba_3SiO$ compounds exhibit poor thermoelectric performance as reflected by their low *ZT* value from 300 K to 1000 K. In contrast, $Ca_3SiO$ exhibits better thermoelectric performance compared to $Ba_3SiO$, which is contributed from the higher electrical conductivity.

### 3.3.9. Correlation of X Cations with Figure of Merit

Figure 14 depicts the correlation of X cations with *ZT* for $Ba_3SiO$ and $Ca_3SiO$ compounds. It can be seen that the substitution of X cations exhibit increasing trend of *ZT* value from 300 K to 1000 K. Among these compounds, the substitution of $Ca^{2+}$ resulting in the highest *ZT* compared to $Ba^{2+}$. This result is influenced by a favorable balance among its transport properties, including Seebeck coefficient, electrical conductivity, and thermal conductivity. The overall enhancement in *ZT* of $Ca_3SiO$ is primarily driven by the higher electrical conductivity compared to $Ba_3SiO$.

## 3.4. Optical Properties

### 3.4.1. Dielectric Function

Figure 15 shows the calculated dielectric function $\varepsilon_1(\omega)$ for $Ba_3SiO$ and $Ca_3SiO$ compounds. In general, the dielectric function of materials includes two parts: the real part, $\varepsilon_1(\omega)$ and imaginary part, $\varepsilon_2(\omega)$. The value of $\varepsilon_1(\omega)$ at the zero frequency, known the static dielectric function $\varepsilon_1(0)$, which defines how well a material can store electrical energy under a constant or low-frequency electric field. The calculated static dielectric values were determined to be 16.94 and 50.07 for $Ba_3SiO$ and $Ca_3SiO$, respectively. Beyond the zero-frequency point, the $\varepsilon_1(\omega)$ function reaches its maximum values. For $Ba_3SiO$, the peak occurs at 1.03 eV with the value of 24.06, while $Ca_3SiO$, the peak appears at 0.10 eV with a much higher value of 80.45. The maximum peak of $\varepsilon_1(\omega)$ exhibit the higher binding of charges, indicates the higher polarity of these compounds. The maximum peak of $\varepsilon_1(\omega)$ also reported by Xiong et. al. in their studied for anti-perovskite $Mg_3XN$ (X = As, Sb, and Bi) [27].

Furthermore, the positive sign of $\varepsilon_1(\omega)$ show that $Ba_3SiO$ and $Ca_3SiO$ have dielectric behaviour. However, when $\varepsilon_1(\omega)$ becomes negative, the materials behaving more a metal, which reflecting light instead of allowing it to pass through. From the $\varepsilon_1(\omega)$ plot, all three compounds show negative values in the visible to ultraviolet region. $Ba_3SiO$ has a negative values from 2.22 eV with dielectric value of −1.43 to 3.15 eV with dielectric value of −1.89 and at 7.59 eV with dielectric value of −1.197, whereas $Ca_3SiO$ shows negative values from 4.39 eV with dielectric value of −3.68 to 7.33 eV with dielectric value of −2.12. This result indicates that these compounds can reflect the light within these energy ranges.

The imaginary part of the dielectric function, $\varepsilon_2(\omega)$, shown by the red curve in Figure 15, represents the energy absorbed by the materials when electrons transition from occupied to unoccupied states. These transitions are known as interband transition. The maximum peak of $\varepsilon_2(\omega)$ is found at 1.36 eV for $Ba_3SiO$, which lies in the visible light region, while the peak for $Ca_3SiO$ appears at 0.32 eV in the infrared region.

To better understanding of these peaks, these $\varepsilon_2(\omega)$ peaks can be correlated to the electronic band structure and PDOS. For both $Ba_3SiO$ and $Ca_3SiO$, the electron transitions mainly happen between the valence band to the conduction band along the Γ – Z k-points, within the energy range of −1.6 eV to 1.6 eV (from electronic band structure plot). The PDOS results further show that these transitions occur from Si-p state to Ba-d for $Ba_3SiO$, Si-p state to Sr-d state for $Sr_3SiO$, and Si-p state to Ca-d state for $Ca_3SiO$. These findings suggest that the $X_3SiO$ (X = Ba and Ca) compounds can

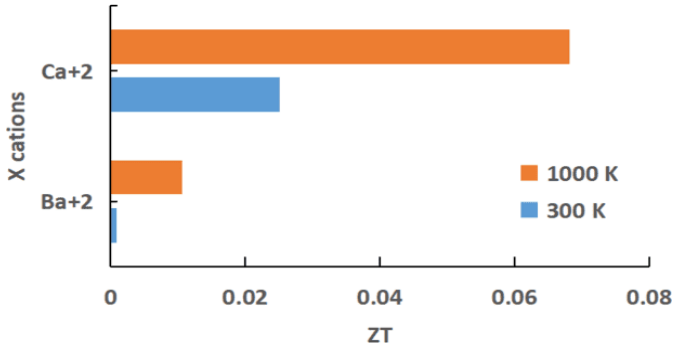


**Figure 14**. Correlation of X cations with figure of merit for $Ba_3SiO$ and $Ca_3SiO$ compounds

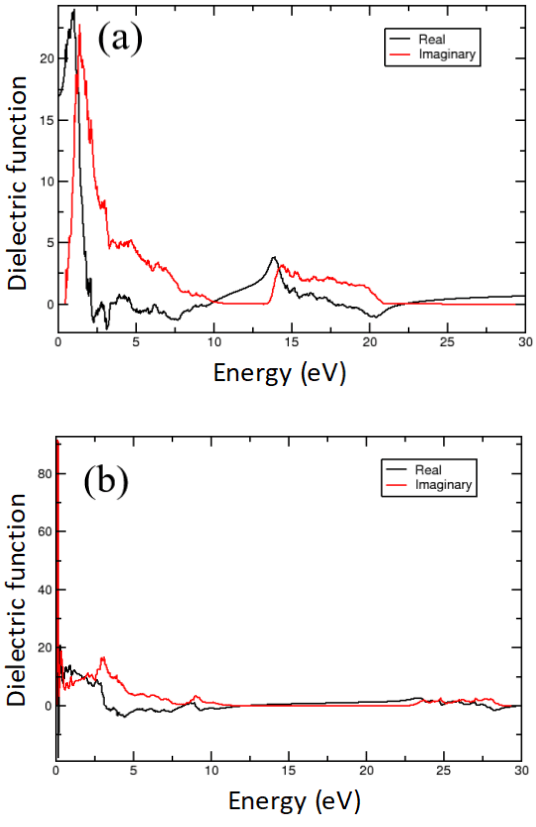


**Figure 15**. Calculated dielectric function of (a) $Ba_3SiO$ and (b) $Ca_3SiO$

interact with the light across infrared (IR) to visible regions. The onset points in $\varepsilon_2(\omega)$ are also found at 0.47 eV and 0.08 eV for $Ba_3SiO$ and $Ca_3SiO$, respectively. These values are close to their band gaps value of 0.44 eV and 0.11 eV for $Ba_3SiO$ and $Ca_3SiO$, respectively, further conforming their semiconductor behavior.

### 3.4.2. Absorption Coefficient

Figure 16 shows the absorption coefficient of $Ba_3SiO$ and $Ca_3SiO$. A higher absorption coefficient of solid materials usually means the material is more efficient at absorbing light and exciting electrons from valence band to conduction band. The absorption curve starts from zero and increases in the visible region (from 1.63 eV to 3.26 eV). In the high ultraviolet region (~18 eV), the highest absorption peaks are observed. For $Ba_3SiO$, the peak occurs at 20.02 eV with $2.31\times 10^8$ $m^{-1}$ absorption. For $Ca_3SiO$, the peak is found at 28.15 eV with $3.98 \times 10^8$ $m^{-1}$ absorption. These values show that $Ba_3SiO$ and $Ca_3SiO$ detect strongly in high ultraviolet regions, suggesting these compounds for ultraviolet detector application.

From visible to ultraviolet regions (1.5 eV to 6.2 eV), the distinct peaks are also observed. However, the higher absorption peaks are determined with values of $8.01 \times 10^8$ $m^{-1}$ (at 6.01 eV) for $Ba_3SiO$ and $9.49 \times 10^8$ $m^{-1}$ (at 6.09 eV) for $Ca_3SiO$. From absorption curve, there are critical onset points of 0.45 eV and 0.094 eV for $Ba_3SiO$ and $Ca_3SiO$, respectively. These onset points correlated with the band gaps of 0.44 eV and 0.11 eV for $Ba_3SiO$ and $Ca_3SiO$, respectively, which again supporting their classification as semiconductor materials.

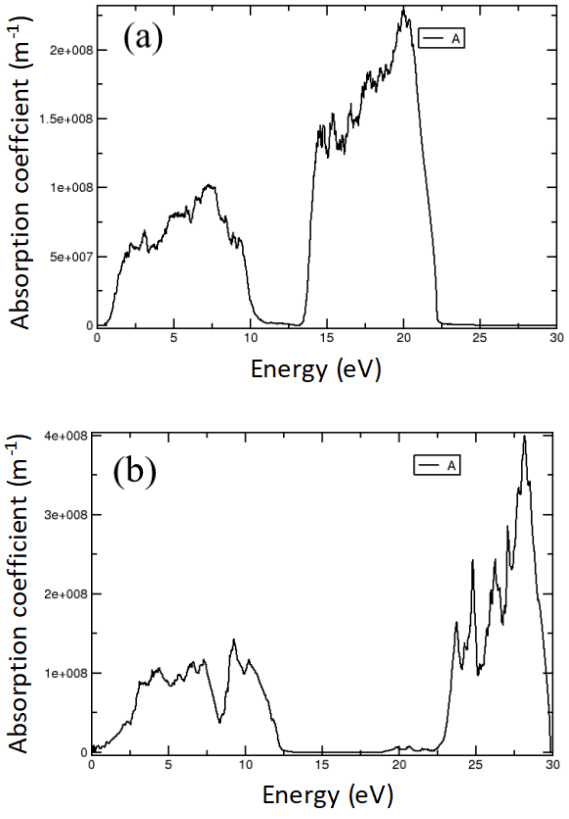


**Figure 16**. Absorption coefficient of (a) $Ba_3SiO$ and (b) $Ca_3SiO$

## 4. CONCLUSION

The anti-perovskite materials $Ba_3SiO$ and $Ca_3SiO$ were investigated using the density functional theory (DFT) method. The band structure analysis shows that both $Ba_3SiO$ and $Ca_3SiO$ are semiconductor materials at the Γ - Γ k-points with direct band gaps of 0.44 eV and 0.11 eV, respectively. For thermoelectric property analysis, $Ba_3SiO$ is identified as an n-type semiconductor material and $Ca_3SiO$ exhibited a p-type semiconductor material at 300 K. In particular, $Ca_3SiO$ showed a high figure of merit ($ZT$) of $2.50 \times 10^{-2}$, along with high electrical conductivity ($k$) of 5610 $(\Omega\cdot m)^{-1}$ compared to $Ba_3SiO$ at this temperature. The substituting of X cations from Ba to Ca in $X_3SiO$ compound increasing the figure of merit from $9.66 \times 10^{-4}$ and $2.50 \times 10^{-2}$, respectively. Furthermore, the lower band gap of $Ca_3SiO$ also shows a good potential for optical applications. From optical property analysis, $Ca_3SiO$ exhibited higher dielectric function with the value of 80.45 in infrared (IR) region and higher absorption with the values of $2.31 \times 10^8$ $m^{-1}$ in ultraviolet region compared to $Ba_3SiO$. This higher absorption within ultraviolet region suggests $Ca_3SiO$ for ultraviolet detector application.

## ACKNOWLEDGMENTS

This work was funded by the Ministry of Higher Education (MoHE) through the Fundamental Research Grant Scheme (FRGS/1/2022/STG05/UNIMAP/01/1). We also express our gratitude to the Malaysia government for supporting this work through the self-funded research grant. MyBrain15 program and research grant, L00022 provided by the Ministry of Science, Technology, and Innovation (MOSTI).

## REFERENCES

[1] S. Twaha, J. Zhu, Y. Yan, and B. Li, "A comprehensive review of thermoelectric technology: Materials, applications, modelling and performance improvement," *Renewable and Sustainable Energy Reviews*, vol. 65, pp. 698–726, 2016, doi: 10.1016/j.rser.2016.07.034.

[2] L. Yang, Z. Chen, M. S. Dargusch, and J. Zou, "High Performance Thermoelectric Materials: Progress and Their Applications," *Advanced Energy Materials*, vol. 8, no. 6, 2018, doi: 10.1002/aenm.201701797.

[3] A. A. Adewale, A. Chik, R. M. Zaki, F. C. Pa, Y. C. Keat, and N. H. Jamil, "DFT Study of Thermoelectric Performance of $SrTiO_3$ Doped by Tantalum," *International Journal of Nanoelectronics and Materials*, vol. 12, no. 4, pp. 477–484, 2019.

[4] Y. Pei, A. D. LaLonde, H. Wang, and G. J. Snyder, "Low effective mass leading to high thermoelectric performance," *Energy & Environmental Science*, vol. 5, no. 7, p. 7963, 2012, doi: 10.1039/c2ee21536e.

[5] X. Li, Y. Zhang, W. Kang, Z. Yan, Y. Shen, and J. Huo, "Anti-perovskite nitrides and oxides: Properties and preparation," *Computational Materials Science*, vol. 225, p. 112188, 2023, doi: 10.1016/j.commatsci.2023.112188.

[6] A. Bali, E. Royanian, E. Bauer, P. Rogl, and R. Chandra Mallik, "Thermoelectric properties of PbTe with encapsulated bismuth secondary phase," *Journal of Applied Physics*, vol. 113, no. 12, 2013, doi: 10.1063/1.4796148.

[7] A. D. LaLonde, Y. Pei, H. Wang, and G. Jeffrey Snyder, "Lead telluride alloy thermoelectrics," *Materials Today*, vol. 14, no. 11, pp. 526–532, 2011, doi: 10.1016/S1369-7021(11)70278-4.

[8] I. Terasaki, "Research Update: Oxide thermoelectrics: Beyond the conventional design rules," *APL Materials*, vol. 4, no. 10, 2016, doi: 10.1063/1.4954227.

[9] W. Liu, L. Yang, Z. Chen, and J. Zou, "Promising and Eco-Friendly $Cu_2$ X-Based Thermoelectric Materials: Progress and Applications," *Advanced Materials*, vol. 32, no. 8, 2020, doi: 10.1002/adma.201905703.

[10] Y. Thimont, L. Presmanes, V. Baylac, P. Tailhades, D. Berthebaud, and F. Gascoin, "Thermoelectric Higher Manganese Silicide: Synthetized, sintered and shaped simultaneously by selective laser sintering/Melting additive manufacturing technique," *Materials Letters*, vol. 214, pp. 236–239, 2018, doi: 10.1016/j.matlet.2017.12.026.

[11] Y. Zhao, C. Lian, S. Zeng, Z. Dai, S. Meng, and J. Ni, "Anomalous electronic and thermoelectric transport properties in cubic $Rb_3AuO$ antiperovskite," *Physical Review B*, vol. 102, no. 9, p. 094314, 2020, doi: 10.1103/PhysRevB.102.094314.

[12] S. Hamada *et al.*, "Prediction of structural, elastic, electronic and thermoelectric properties of the $Rb_3CuO$ and $Rb_3AgO$ anti-perovskites," *Computational Condensed Matter*, vol. 36, p. e00834, 2023, doi: 10.1016/j.cocom.2023.e00834.

[13] X. He *et al.*, "Inverse-Perovskite $Ba_3BO$ ( $B$ = Si and Ge) as a High Performance Environmentally Benign Thermoelectric Material with Low Lattice Thermal Conductivity," *Advanced Science*, vol. 11, no. 10, 2024, doi: 10.1002/advs.202307058.

[14] J.-H. Pöhls and A. Mar, "Thermoelectric properties of inverse perovskites $A_3TtO$ ($A$ = Mg, Ca; $Tt$ = Si, Ge): Computational and experimental investigations," *Journal of Applied Physics*, vol. 126, no. 2, 2019, doi: 10.1063/1.5095247.

[15] S. J. Clark *et al.*, "First principles methods using CASTEP," *Zeitschrift für Kristallographie - Crystalline Materials*, vol. 220, no. 5–6, pp. 567–570, 2005, doi: 10.1524/zkri.220.5.567.65075.

[16] G. K. H. Madsen and D. J. Singh, "BoltzTraP. A code for calculating band-structure dependent quantities," *Computer Physics Communications*, vol. 175, no. 1, pp. 67–71, 2006, doi: 10.1016/j.cpc.2006.03.007.

[17] A. Togo, L. Chaput, T. Tadano, and I. Tanaka, "Implementation strategies in phonopy and phono3py," *Journal of Physics: Condensed Matter*, vol. 35, no. 35, p. 353001, 2023, doi: 10.1088/1361-648X/acd831.

[18] J. P. Perdew, K. Burke, and M. Ernzerhof, "Generalized Gradient Approximation Made Simple," *Physical Review Letters*, vol. 77, no. 18, pp. 3865–3868, 1996, doi: 10.1103/PhysRevLett.77.3865.

[19] G. I. Csonka *et al.*, "Assessing the performance of recent density functionals for bulk solids," *Physical Review B*, vol. 79, no. 15, p. 155107, 2009, doi: 10.1103/PhysRevB.79.155107.

[20] F. Birch, "Finite Elastic Strain of Cubic Crystals," *Physical Review*, vol. 71, no. 11, pp. 809–824, 1947, doi: 10.1103/PhysRev.71.809.

[21] B. Huang and J. D. Corbett, "Orthorhombic Inverse Perovskitic Ba3TtO (Tt = Ge, Si) as Zintl Phases," *Zeitschrift für anorganische und allgemeine Chemie*, vol. 624, no. 11, pp. 1787–1790, 1998, doi: 10.1002/(SICI)1521-3749(1998110)624:11<1787::AID-ZAAC1787>3.0.CO;2-P.

[22] Q. Mahmood, A. Ashraf, and M. Hassan, "Investigations of optical and thermoelectric response of direct band gap $Ca_3XO$ (X = Si, Ge) anti-perovskites stabilized in cubic and orthorhombic phases," *Indian Journal of Physics*, vol. 92, no. 7, pp. 865–874, Jul. 2018, doi: 10.1007/s12648-018-1177-5.

[23] S. M. Alqahtani, A. Q. Alsayoud, and F. H. Alharbi, "Structures, band gaps, and formation energies of highly stable phases of inorganic $ABX_3$ halides: A = Li, Na, K, Rb, Cs, Tl; B = Be, Mg, Ca, Ge, Sr, Sn, Pb; and X = F, Cl, Br, I," *RSC Advances*, vol. 13, no. 13, pp. 9026–9032, 2023, doi: 10.1039/D3RA00185G.

[24] A. C. Garcia-Castro, R. Ospina, and J. H. Quintero, "Octahedral distortion and electronic properties of the antiperovskite oxide Ba3SiO: First principles study," *Journal of Physics and Chemistry of Solids*, vol. 136, p. 109126, 2020, doi: 10.1016/j.jpcs.2019.109126.

[25] U. Rani, P. K. Kamlesh, A. Shukla, and A. S. Verma, "Emerging potential antiperovskite materials $ANX_3$ (A= P, As, Sb, Bi; X= Sr, Ca, Mg) for thermoelectric renewable energy generators," *Journal of Solid State Chemistry*, vol. 300, p. 122246, 2021, doi: 10.1016/j.jssc.2021.122246.

[26] S. Sk, N. Shahi, and S. K. Pandey, "Experimental and computational approaches to study the high temperature thermoelectric properties of novel topological semimetal CoSi," *Journal of Physics: Condensed Matter*, vol. 34, no. 26, p. 265901, 2022, doi: 10.1088/1361-648X/ac655a.

[27] M. Xiong, S. Wang, and Z. Mao, "Regarding the structural, thermodynamic, mechanical, thermoelectric, and optoelectronic properties of anti-perovskite $Mg_3XN$ (X = As, Sb, and Bi) through a DFT approach," *Physica B: Condensed Matter*, vol. 683, p. 415892, 2024, doi: 10.1016/j.physb.2024.415892.

[28] N. W. Ashcroft and N. D. Mermin, *Solid State Physics*. Philadelphia, PA, USA: Saunders College Publishing, 1976.

[29] G. J. Snyder and E. S. Toberer, "Complex thermoelectric materials," *Nature Materials*, vol. 7, no. 2, pp. 105–114, 2008, doi: 10.1038/nmat2090.

[30] M. Moakafi, R. Khenata, A. Bouhemadou, F. Semari, A. H. Reshak, and M. Rabah, "Elastic, electronic and optical properties of cubic antiperovskites SbNCa3 and BiNCa3," *Computational Materials Science*, vol. 46, no. 4, pp. 1051–1057, 2009, doi: 10.1016/j.commatsci.2009.05.011.

[31] S. Hasan, S. San, K. Baral, N. Li, P. Rulis, and W.-Y. Ching, "First-Principles Calculations of

Thermoelectric Transport Properties of Quaternary and Ternary Bulk Chalcogenide Crystals," *Materials*, vol. 15, no. 8, p. 2843, 2022, doi: 10.3390/ma15082843.

[32] F. U. Parás-Hernández, A. Fabián-Mijangos, M. A. Cardona-Castro, and J. Alvarez-Quintana, "Enhanced performance nanostructured thermoelectric converter for self-powering health sensors," *Nano Energy*, vol. 74, p. 104854, 2020, doi: 10.1016/j.nanoen.2020.104854.